Evaluating four remote sensing based models to estimate latent heat flux in semi-arid climate for heterogeneous surface coverage of western Algeria

Tewfik A. Oualid ✉ iD, Abderrahmane Hamimed iD, Abdelkader Khaldi iD

University Mustapha Stambouli of Mascara, Laboratory of Biological Systems and Geomatics,
P.O. Box 305, Route de Mamounia, 29000, Mascara, Algeria

Abstract: Optimal estimation of water balance components at the local and regional scales is essential for many applications such as integrated water resources management, hydrogeological modelling and irrigation scheduling. Evapotranspiration is a very important component of the hydrological cycle at the soil surface, particularly in arid and semi-arid lands. Mapping evapotranspiration at high resolution with internalised calibration (METRIC), trapezoid interpolation model (TIM), two-source energy balance (TSEB), and soil-plant-atmosphere and remote sensing evapotranspiration (SPARSE) models were applied using Landsat 8 images for four dates during 2014–2015 and meteorological data. Surface energy maps were then generated. Latent heat flux estimated by four models was then compared and evaluated with those measured by applying the method of Bowen ratio for the various days. In warm periods with high water stress differences and with important surface temperature differences, METRIC proves to be the most robust with the root-mean-square error ($RMSE$) less than 40 W·m^{-2}. However, during the periods with no significant surface temperature and soil humidity differences, SPARSE model is superior with the $RMSE$ of 35 W·m^{-2}. The results of TIM are close to METRIC, since both models are sensitive to the difference in surface temperature. However, SPARSE remains reliable with the $RMSE$ of 55 W·m^{-2} unlike TSEB, which has a large deviation from the other models. On the other hand, during the days when the temperature difference is small, SPARSE and TSEB are superior, with a clear advantage of SPARSE serial version, where temperature differences are less important.

Keywords: Algeria, energy balance, evapotranspiration, Landsat, METRIC, SPARSE, TIM, TSEB

INTRODUCTION

Evapotranspiration (ET) is the important element of hydrological balance; it accounts for almost two-thirds of the global return of precipitation to the atmosphere [Brutsaert 1982]. This proportion is higher in arid and semi-arid regions [Chehbouni *et al.* 2008]. In these regions, irrigation consumes more than 80% of the available water [WWAP 2012]. However, the efficiency of this use could be well improved by reducing water losses through evaporation into the atmosphere, infiltration to groundwater and by good calculation of irrigation water requirements. This optimisation of water use has a significant impact on agricultural productivity by reducing costs and increasing production. Evapotranspiration (ET) can be measured over time and at a given point in an agricultural plot, but it is very difficult or impossible to measure on a large scale, such as in the watershed. Remote sensing is an appropriate tool for this monitoring, as it allows the spatialisation of ET by monitoring vegetation growth or by detecting water stress.

Many studies have compared and evaluated the remotely sensed-based models. This studies have shown a large difference in the results of latent heat flux compared to ground data, with root-mean-square errors ($RMSE$) ranging from 60 W·m^{-2} [Timmermans *et al.* 2007] to 150 W·m^{-2} [Choi *et al.* 2009]. The differences can be explained by several factors such as the poor adaptation of these algorithms to the fields studied (for example, the Priestley-Taylor parameter (α) used for estimating the latent heat flux (LE) from vegetation ranging from 1.26 to 1.8 depending on climate, or the *xg*

coefficient for estimating soil heat flux G ranging from 0.2 to 0.4). So, the contextual models are very sensitive to the difference in surface temperature between the two extremes (dry and wet boundary). These models lead to erroneous results when the difference between surface and air temperature is low, or the sensitivity of pixel-by-pixel models to the vegetation index ($NDVI$), with LE values exploding in extremes, or even atmospheric corrections that rely on algorithms adapted to regions and not others as well as the quality of infrared images, poses problems for some sensors like the band 11 of Landsat 8 thermal infrared sensor (TIRS). These errors in the estimation of surface temperature (T_s) can also lead to errors in the estimation of surface emissivity (1% error in the emissivity value causes an underestimate of T_s of approximately 0.4 to 0.8°C) [VIDAL, PERRIER 1990].

region is part of the immense plain of the Macta (Fig. 1) with an area of 14,500 km^2 [BENZATER et al. 2019], communicating with the Mediterranean Sea by a narrow channel. The soils of the Habra plain consist of sedimentary formation with variable texture: alluvial-colluvial, alluvial, or rarely colluvial. These formations are distributed in less regular and homogeneous entities with a salinity of 8–16 mS·cm^{-1} at a depth greater than 50 cm and with low leaching [FELLAH et al. 2021]. The study site is located in a semi-arid area of a Mediterranean climate characterised by a wet and cold period (minimum air temperature (T_a) lies between 6 and 8°C) in late fall and winter, and another dry and warm period (maximum T_a about 42°C) in late spring and summer. The average annual rainfall is approximately 450 mm [ELOUISSI et al. 2017].
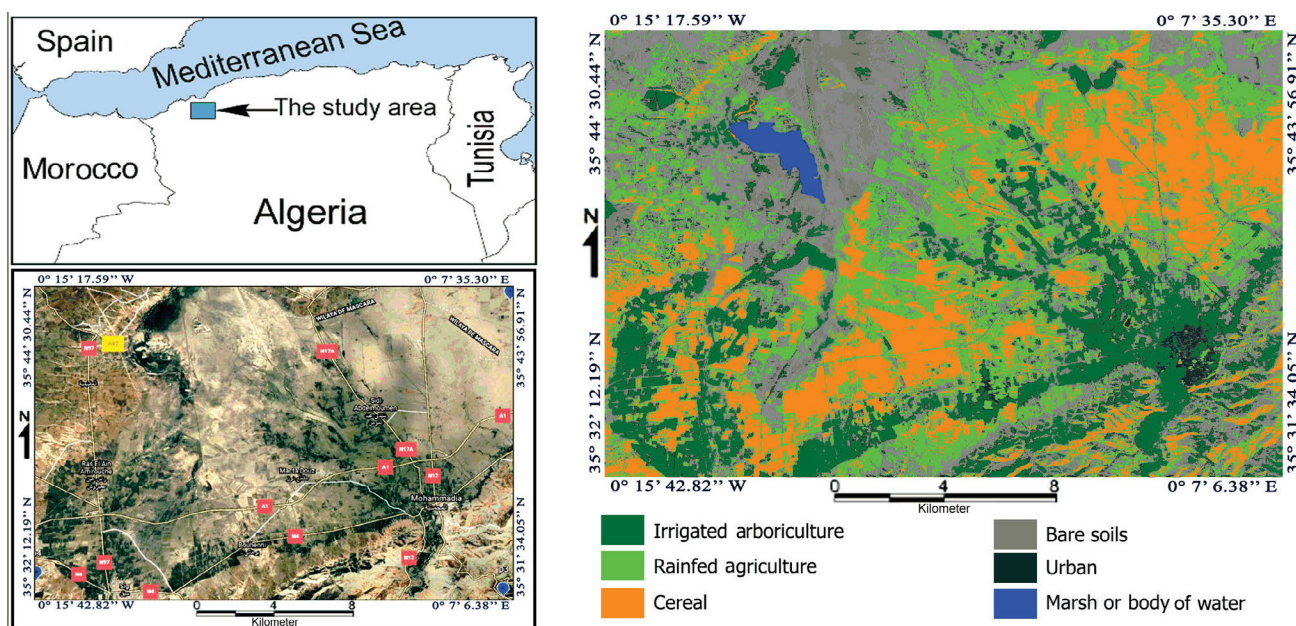
Fig. 1. Location and land use land cover of Landsat 8 imagery acquired on September 1, 2014 (DOY 244) of the study area; DOY = day of year; source: own elaboration based on Landsat satellite images from Earth Explorer [USGS undated a]

The objective of this work is to compare and evaluate the relative performance of four thermal infrared (TIR) algorithms derived from remote sensing data over an irrigated perimeter in a semi-arid climatic context with heterogeneous land cover to estimate surface energy flux, including latent heat flux, which can be converted into actual daily ET and water stress degree in order to provide an adequate and effective solution to water managers and especially irrigation scheduling.

The choice of this selected area is dictated by the existence of two water extremes between wet and dry lands, in particular the marshes of Macta and the irrigated parcels of Habra, and by the availability of agrometeorological data at the stations located on the study site, namely the Mohammadia, Shaouria, Bouhenni and Sidi Abdelmoumen stations, and its virtually flat topography, which greatly simplifies the application of the four models.

MATERIALS AND METHODS

STUDY AREA

For this work, we have selected a pilot site which corresponds to the agricultural areas of the plain of Habra and which is a sub-littoral depression of Oran. This site is located in the north-west of Algeria between the longitudes 0°15'42" W and 0°7'6" E and latitudes 35°31'34" N and 35°44'30" N (Fig. 1). This plain houses the irrigated perimeter of Mohammadia, known by citrus cultivation and also called "the plain of citrus fruits". The selected

DATA USED

Meteorological data

The meteorological data used in this study (Tab. 1) are obtained from the network of the National Office of Meteorology (Fr. Office National de Météorologique, ONM) and the National Water Resources Agency (Fr. Agence Nationale des Ressources Hydrauliques, ANRH). However, data from Mohammadia, Sidi Abdelmoumen, Menasria and Shaouria ONM meteorological stations are used, with the Landsat 8 satellite measurements, to characterise the water status over the Habra plain.

Table 1. Meteorological conditions during the image acquisition of Landsat 8 OLI/TIRS on the selected days

Parameter at 10H38 (GMT)	Unit	01.09.2014 (DOY 244)	19.10.2014 (DOY 292)	22.12.2014 (DOY 356)	12.03.2015 (DOY 071)
Relative humidity	%	34.4	18	79	40
Air temperature	°C	31	32.8	11.9	21.1
Incoming shortwave radiation	$W \cdot m^{-2}$	796	647	431	740
Atmospheric pressure	kPa	101.32	101.26	102.46	101.47
Atmospheric radiation	$W \cdot m^{-2}$	402	331	246	388
Wind speed	$m \cdot s^{-1}$	3	1.8	0.4	1.8
Atmospheric transmittance	–	0.73	0.71	0.75	0.77
Relative sunshine duration	–	0.83	0.81	0.62	0.69
Potential evapotranspiration	mm	4.05	5.31	1.02	4.61

Explanations: 10H38 = 10 h 38 min, GMT = Greenwich Mean Time, DOY = day of year.
Source: own elaboration based on National Office of Meteorology and the National Water Resources Agency.

The available data are:
– air temperature at 2 m at the scale of the minute for the satellite shooting days;
– soil temperatures (0.5 and 1 m);
– daily rainfall of the month of satellite shooting days;
– psychrometric temperatures at 2 m (wet thermometer and dry thermometer);
– dew point temperature;
– air water vapour pressure;
– atmospheric pressure;
– air relative humidity;
– global radiation at hourly intervals of satellite shooting days;
– wind speed at 2 m.

Validation data

Validation data are the air temperature at 0.5 and 2.5 m (chromel-alumel thermocouples) and the relative humidity at 0.5 and 2.5 m (Vaisala capacitive sensors, Model HMP35D).

Satellite data

The use of satellite data has the advantage of providing near-daily spatio-temporal tracking of most variables of the soil-vegetation-atmosphere interface. These are variables characteristic of the atmosphere (radiative, thermodynamic and mechanical), vegetation (structural, radiative and physiological) and soil (thermodynamic and hydraulic). The satellite dataset consists of four images acquired by the Landsat 8 OLI/TIRS satellite sensor between September 2014 and March 2015.

PREPROCESSING OF SATELLITE IMAGES

Atmospheric correction in the visible, and near infrared bands

Radiometric and atmospheric corrections were made using FLAASH (fast line-of-sight atmospheric analysis of spectral hypercubes) ENVI software module. This is a correction approach using five-dimensional look-up tables (LUT) [Kaufman et al. 1997; Staenz et al. 2002], namely the wavelength, the pixel position, atmospheric water, terrain elevation and optical thickness of the atmosphere at 550 nm. The latter is estimated

Table 2. The spectral bands of Landsat 8 OLI/TIRS instrument

Spectral band	Wavelength (μm)	Resolution (m)
1 – aerosols	0.433–0.453	30
2 – blue	0.450–0.515	30
3 – green	0.525–0.600	30
4 – red	0.630–0.680	30
5 – near infrared	0.845–0.885	30
6 – medium infrared 1	1.560–1.660	30
7 – medium infrared 2	2.100–2.300	30
8 – panchromatic	0.500–0.680	15
9 – cirrus	1.360–1.390	30
10 – medium infrared	10.30–11.30	100
11 – medium infrared	11.50–12.50	100

Source: own elaboration based on Landsat Missions [USGS undated b].

according to visibility (meteorological data). MODTRAN 4 radiative transfer algorithm [Berk et al. 1999] is used for the estimation of surface reflectance.

Atmospheric correction in the thermal infrared

Several methods exist to correct satellite data in the thermal infrared (TIR) of atmospheric effects. We can either use a radiative transfer code in the atmosphere such as MODTRAN (moderate spectral atmospheric resolution transmittance) [Berk et al. 1999] to estimate the various contributions of the atmosphere, or we can use semi-automatic methods. Empirical studies are based on differences in absorption by the atmosphere between two near spectral bands, this is the case of the split-window method. In this work, we chose to use the MODTRAN 4 atmospheric radiative transfer code to correct the radiance in the TIR Landsat sensor.

Determination of input parameters

On-board radiometers measure spectral radiance in the visible, near infrared, mid-infrared and thermal infrared at the top of the atmosphere; these elementary radiance data are converted into albedo (r), vegetation index ($NDVI$) and surface temperature (T_s). The data used are Landsat 8 OLI/TIRS imagery. The spectral bands of the two sensors are provided in digit number (encoded in 8-bit) which are transformed into exo-atmospheric spectral radiance ($L\uparrow_{\text{sat}}(\lambda)$) in the optical and thermal domains. We use the linear formula:

$$L\uparrow_{\text{sat}}(\lambda) = A\,CN + B \qquad (1)$$

where: $L\uparrow_{\text{sat}}(\lambda)$ = exo-atmospheric spectral radiance, CN = the digit number, A and B = the calibration coefficients.

Spectral radiance is converted after atmospheric correction into surface reflectance then this later is used to calculate albedo (r) and vegetation index ($NDVI$).

The albedo (r) is calculated by the adapted (for Landsat 8) formula proposed by Liang et al. [2002]:

$$r = 0.356r_2 + 0.13r_4 + 0.373r_5 + 0.085r_6 + 0.072r_7 - 0.0018 \quad (2)$$

where: r = albedo, r_2, r_4, r_5, r_6 and r_7 = respectively the reflectance in bands 2, 4, 5, 6 and 7 of Landsat 8.

The vegetation index is calculated from surface reflectance in red and near infrared. The values obtained for a terrestrial surface are significant and correspond to physical reality (0–1), unlike those obtained from the digit number. Normalised vegetation index was calculated using the following equation:

$$NDVI = \frac{NIR - R}{NIR + R} \qquad (3)$$

which corresponds in the case of Landsat 8 to:

$$NDVI = \frac{r_5 - r_4}{r_5 + r_4} \qquad (4)$$

where: $NDVI$ = normalised difference vegetation index, NIR = near infrared band, R = red band, r_4, r_5 = respectively the reflectance in the bands 4 and 5 of Landsat 8.

Surface temperature

The surface temperature (T_s) is deduced from the thermal infrared spectral radiance ($L\uparrow_{\text{sat}}(\lambda)$). This later is expressed by using the following equation [Barsi et al. 2005]:

$$L\uparrow_{\text{sat}}(\lambda) = [\varepsilon_o L_\lambda(T_s) + (1 - \varepsilon_o)L\downarrow_{\text{atm}}(\lambda)]\tau_\lambda + L\uparrow_{\text{atm}}(\lambda) \qquad (5)$$

where: $L_\lambda(T_s)$ = spectral radiance of the surface, τ_λ = spectral transmissivity of the atmosphere, $L\downarrow_{\text{atm}}(\lambda)$ = atmospheric radiation received by the surface, $L\uparrow_{\text{atm}}(\lambda)$ = radiation received by the sensor, ε_o = surface emissivity that is estimated as a logarithmic (log) function of $NDVI$ vegetation index using Van De Griend and Owe [1993] formula:

$$\varepsilon_o = 1.0094 + 0.047 log(NDVI) \qquad (6)$$

Atmospheric parameters (τ_λ, $L\downarrow_{\text{atm}}(\lambda)$, $L\uparrow_{\text{atm}}(\lambda)$) are calculated using the on-line atmospheric correction parameters calculator

[Barsi et al. 2005]. These parameters make it possible to deduce the corrected spectral radiance of the surface ($L_\lambda(T_s)$) by inversion of the Equation (5). The surface temperatures (T_s) are finally obtained as a function of these radiances using Planck's formula [Chander et al. 2009]:

$$T_s = \frac{1321.08}{\log\left(\frac{774.89}{L_\lambda(T_s)} + 1\right)} \qquad (7)$$

MODELS

The estimation of optical and thermal remote sensing ET has been the subject of many methodological approaches over the past thirty years. Several approaches have been developed using optical and thermal remote sensing to estimate ET, next, we cite three categories of models.

1. Models that use simple semi-empirical relationships to link daily ET to instantaneous surface temperature measurement [Seguin, Itier 1983]. The advantage of these models is to circumvent three problems: a) estimation of surface roughness lengths (involved in the sensitive heat flux), b) lack of continuous measurement of surface temperatures, c) estimation of soil heat flux which is negligible on a daily basis. However, they have limitations related to the low spatial representativeness of air temperature, measured locally, and the difficulty of taking into account the heterogeneity of a surface. Unlike thermal infrared methods, these models are also based on the assumption that the $H{:}R_n$ ratio, a relative sensible heat flux to net radiation, is constant during the day and that the soil heat flux G is negligible on the day scale.

2. Models that use deterministic relationships based on a detailed description of soils and vegetation cover [Olioso et al. 1999]. These models are often referred to as soil-vegetation-atmosphere transfer (SVAT) and can simulate surface temperature from irrigation inputs and precipitation [Chirouze et al. 2014]. These models, which are difficult to implement on a large scale because of the lack of information on irrigation, do not depend on remote sensing data for their implementation. However, remote sensing data can be assimilated into these models [Olioso, Jacob 2002] and simulate mass and energy transfers between soil, vegetation and atmosphere on time scales of less than one hour, in accordance with the dynamics of atmospheric and surface processes; however, these models are highly parameterised and require information on water supply, especially irrigation.

3. Methods that use remote sensing data in the thermal infrared domain (3–15 μm) to calculate the instantaneous ET at the time of the satellite's upper passage, which can be converted into daily values using algorithmic extrapolation as an evaporation fraction. These methods can be divided into two groups described next.

- Single source contextual models are developed to solve the energy balance equation by linking current pixel conditions to sites under extreme water conditions (very dry and very wet) for various vegetation cover conditions. The properties of these sites are used to determine some soil-vegetation-atmosphere interface variables that are not accessible by remote sensing [Hamimed et al. 2009]. A well-calibrated single source model may well surpass a poorly configured double source model

[KUSTAS, DAUGHTRY 1990]. These models use the pixel values of a given image and interpolate the *ET* values between the two extremes to provide intermediate *ET* values, however, they have a weakness when extreme water conditions are not present in the image, especially in agricultural areas with sufficient irrigation or when applied to satellite images with a low spatial resolution where the surface temperature is an average pixel. In this group we can mention simple models such as TIM (trapezoid interpolation model), TS–VI (surface temperature–vegetation index triangle method), and S-SEBI (simplified surface energy balance index) or complexes such as SEBS (surface energy balance system), SEBAL (surface energy balance algorithm for land) and METRIC (mapping *ET* with internalised calibration).

- Single pixel methods are adapted to high and low spatial resolution images, they allow us to estimate *ET* by solving the energy balance equation for each pixel independently of the others. In this group we can mention models such as TSEB (two-source energy balance) and SPARSE (soil plant atmosphere and remote sensing *ET*). However, these models are generally expected to be well adapted to uniform landscapes with fairly homogeneous vegetation and surface water conditions [CHIROUZE et al. 2014]. In this study, four models are analysed and evaluated over the Habra plain using the Landsat 8 OLI/TIRS images.

Mapping *ET* at high resolution with internalised calibration (METRIC)

Like all the residual models, METRIC estimates *ET* based on the resolution of the energy balance equation, the latent heat flux (*LE*) as the residual term (Tab. 3):

Table 3. Symbols used in this study.

Symbol	Unit	Description
Cp	$J \cdot kg^{-1} \cdot K^{-1}$	air specific heat at constant pressure
d	m	displacement height
dT	K	near-surface temperature difference
e_a		air vapour pressure at reference level
e_0	Pa	air vapour pressure at the aerodynamic level
$e_{sat}(T_x)$		saturated vapour pressure at temperature T_x
EF	–	evaporative fraction
ET		evapotranspiration
ET_o		daily reference evapotranspiration
ET_{inst}	$mm \cdot h^{-1}$	instantaneous evapotranspiration
ET_j		daily evapotranspiration
ET_{hor}		hourly evapotranspiration
f_c	–	fraction cover
g	$m \cdot s^{-2}$	acceleration due to gravity
G	$W \cdot m^{-2}$	soil heat flux
H		sensible heat flux
k	–	von Karman's constant (= 0.41)
L	m	Monin-Obukhov length
$L\downarrow$		incoming longwave radiation
$L\uparrow$	$W \cdot m^{-2}$	emitted outgoing longwave radiation
LE		latent heat flux
LE_s		soil latent heat flux

cont. Tab. 3

Symbol	Unit	Description
LE_c		canopy latent heat flux
m		coefficient of the stability function
n_{sw}	–	coefficient in r_{av}
$NDVI$		normalised difference vegetation index
r, r_0		surface albedo
r_a		aerodynamic resistance between the aerodynamic level and the reference level
r_{ah}		aerodynamic resistance to heat transport
r_{as}	$s \cdot m^{-1}$	aerodynamic resistance between the soil and the aerodynamic level
r_{av}		aerodynamic resistance between the vegetation and the aerodynamic level
r_g	$W \cdot m^{-2}$	net radiation over the soil
r_{sl}		surface resistance to evaporation
r_x	$s \cdot m^{-1}$	resistance of the total surface layer boundary layer
R_g		incoming shortwave radiation
R_n		total net radiation at the surface
R_{ns}	$W \cdot m^{-2}$	soil net radiation
R_{nc}		canopy net radiation
T_{atm}		incoming atmospheric radiation
T_s		surface temperature
T_{sl}		soil temperature
T_c		canopy temperature
T_a	K	air temperature
T_{aero}		aerodynamic temperature
T_0, T_{ac}		aerodynamic temperature of the air
T_{rad}		radiative surface temperature
$u^\star$	$m \cdot s^{-1}$	friction velocity
u_{200}		wind speed at blending height (200 m)
x_g	–	coefficient of soil heat flux
z_{om}	m	roughness length for momentum transport
α_0		coefficient in r_{av}
α_s		soil albedo
α_v	–	vegetation albedo
β		evapotranspiration efficiency
βo		Bowen ratio
ρ	$kg \cdot m^{-3}$	air density
φ		Priestley-Taylor parameter
ε_a		atmosphere emissivity
ε_o		surface emissivity
τ	–	atmospheric transmittance
ε_s		soil emissivity
ε_v		vegetation emissivity
φ		parameter similar to the Priestley-Taylor parameter
λ	$J \cdot kg^{-1}$	latent heat of vaporisation of water
γ	$kPa \cdot K^{-1}$	psychrometric constant
Δ		slope of the saturation vapor curve
σ	$W \cdot m^{-2} \cdot K^2$	Stefan–Bolzman constant
ψ_h	–	stability function for heat transport
ψ_m		stability function for momentum transport

Source: own elaboration.

$$LE = R_n - G - H \qquad (8)$$

Net radiation at the surface (R_n) is the balance sheet of the different forms of radiative exchange. It is calculated using formula:

$$R_n = (1 - r)R_g + L\downarrow - L\uparrow \qquad (9)$$

To calculate net radiation we must estimate the following terms: the incoming shortwave radiation R_g (obtained from meteorological observations); this data allowed us to estimate the transmissivity (τ) of the atmosphere, which represents the capacity of the atmosphere to transmit solar radiation. Emission by the surface ($L\uparrow$) was obtained by the Stephan-Boltzmann expression ($L\uparrow = \varepsilon T_s^4$), using the surface temperature (T_s) and the surface emissivity (ε). Long-wave atmospheric radiation ($L\downarrow$) was obtained using air temperature T_a and emissivity of atmosphere. The latter is calculated as a function of the transmissivity of the atmosphere (τ) according to the expression of BASTIAANSSEN *et al.* [1998]:

$$\varepsilon = 1.08[\log(\tau)]^{0.265} \qquad (10)$$

Soil heat flux (G) is calculated from empirical formula of BASTIANSSEN *et al.* [2000]:

$$G = (T_s - 273.15)(0.0038 + 0.0074r)\left[1 - 0.98NDVI^4\right]R_n \quad (11)$$

Landsat 8 data was acquired around 10:30 GMT.

Sensible heat flux (H) is calculated as a function of difference between T_{aero} and surface temperature identical to that on the z_{oh} thermal roughness height and that of T_a:

$$H = [(\rho Cp) : r_{ah}](T_{\text{aero}} - T_a) \qquad (12)$$

where, ρ = density of air at constant pressure, Cp = specific heat of air at constant pressure, r_{ah} = resistance to turbulent transfer, T_{aero} = aerodynamic temperature, T_a = air temperature.

In the METRIC model, sensible heat flux (H) is calculated without needing to know the values of T_{aero} and T_a, difficult to obtain by remote sensing, but rather the difference (dT) between the temperatures T_1 and T_2 (corresponding respectively to the heights $z_1 = 0$, 1 and $z_2 = 2$ m above the surface) which is a function of T_s:

$$H = [(\rho Cp) : r_{ah}]dT \qquad (13)$$

where: dT = near-surface temperature difference, r_{ah} is determined between two atmospheric levels z_1 and z_2 using a wind speed u_{200}, obtained by extrapolation, at the mixing height (z_b) (generally between 50 and 200 m above the surface) and an iterative procedure for the correction of atmospheric stabilities to heat transfer and momentum transfer, based on the Monin-Obukhov theory [PAULSON 1970]. In this work, a mixing height (z_b) of 200 m was used. The difference (dT) between temperatures T_1 and T_2 is calculated using the linear function of T_s:

$$dT = a\,T_s + b \qquad (14)$$

Coefficients a and b are empirically calculated using the triangle of the scatter plot generated by the scatter plot of the vegetation index NDVI and the surface temperature T_s [KHALDI *et al.* 2011]. On bare soils with a high surface temperature, we identify dry pixels and on those with dense vegetation cover and a low temperature we identify wet pixels. Then H dry (H_s) and H wet (H_h) are calculated using the energy balance equation, as follows:

$$H_h = (R_n - G)_h - LE_h \qquad (15)$$

$$H_s = (R_n - G)_s - LE_s \qquad (16)$$

where: H_s = sensible heat flux for the dry pixels, H_h = sensible heat flux for wet pixels, R_n = net radiation at the surface. A dry pixel is characterised by a latent heat flux (LE_s) = 0 and $H = (R_n - G)$. For a wet pixel, latent heat flux (LE_{hor}) = hourly value of the reference ET (ET_r) [ALLEN *et al.* 1998] multiplied by an empirical coefficient of 1.05. The choice of this coefficient is dictated mainly by the assumption that a wet pixel (totally covered by vegetation) generally has a value ET rate of 5% greater than ET_r, due to the presence of moist soil under cover, which will slightly increase total ET [ALLEN *et al.* 2007]. The determination of H_s and H_h allows, by inversion of the Equation (8), to deduce the difference between the temperatures T_1 and T_2 of the dry pixels (dT_s) and that of the wet pixels (dT_h). The coefficients a and b of Equation (15) are calculated using the adjustment of a line passing through the two pairs of values (dT and Ts), corresponding to dry and wet pixels. The use of the expression H then makes it possible to estimate the sensible and latent heat fluxes. The latter must make it possible to interpret more precisely the attitude of the surface compared to water stress. However, its values strongly depend on the conditions of its estimation. Indicators of water stress can be deduced such as the surface resistance to evaporation (r_s), the parameter of Priestley-Taylor (α), and the evaporative fraction of (EF).

Latent heat flux (LE) is then converted into (ET_{inst}) instantaneous ET (in mm·h^{-1} converts from s to h) using the following formula:

$$ET_{\text{inst}} = (3600 : (\rho\lambda))LE \qquad (18)$$

where: ρ = density of water (~1 kg·m^3), λ = latent heat of water vaporisation (~2.45 · 10^6 J·kg^{-1} at 20°C).

Reference ET fraction (ET_{rF}) is calculated from the hourly value of ET (ET_{hor}) and ET_r ratio. It is considered similar to that integrated during the day [GENTINE *et al.* 2011]. The daily evapotranspiration (ET_j) is calculated using from the expression [ALLEN *et al.* 2007]:

$$ET_j = ET_{rF}ET_o \qquad (18)$$

where: ET_o = daily reference ET (mm·d^{-1}) which is calculated by the Penman-Monteith equation [ALLEN *et al.* 1998] using conventional data provided by the weather station.

Trapezoid interpolation model (TIM)

Unlike models that use the energy balance equation to estimate latent heat flux, and because of the complexity of estimating sensible heat flux (H), TIM is a contextual one-layer model based on a simple interpolation method using measurable parameters with remote sensing proposed by [JIANG, ISLAM 2001] which

establishes a link between available energy (R_n – G) and latent heat flux, comparable to the Priestley-Taylor equation:

$$LE = \varphi \frac{\Delta}{\Delta + \gamma} (R_n - G) \tag{19}$$

where: φ = a parameter similar to the Priestley-Taylor parameter (α = 1.26) varying between 0 and 1.26 and depending on the surface water status, γ = the psychrometric constant, generally equal to 0.066 kPa·K^{-1} [Crago, Brutsaert 1992]. The key point of the TIM model is the interpretation of the trapezoidal shape of the scatter plot resulting from interpolation between T_s and NDVI (Fig. 2). Four points of the trapezoid (dry vegetation cover, wet vegetation cover, dry bare soil and moist bare soil) represent the two limits in terms of surface temperature and vegetation cover rate, where they are determined in our experimental work. Net radiation (R_n) was calculated using [Allen et al. 1998] formula:

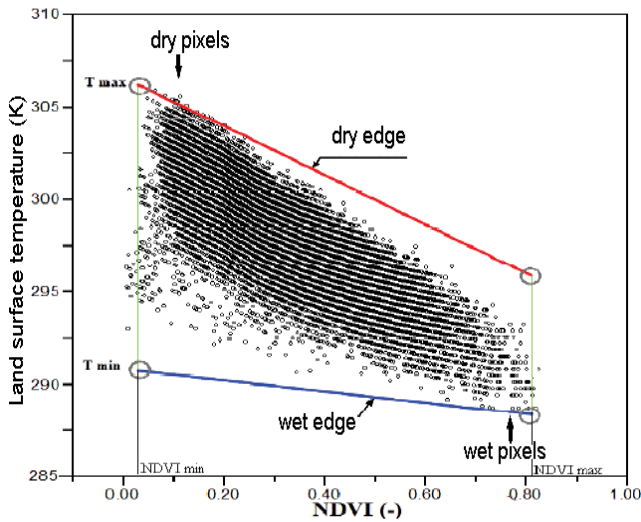$$R_n = (1 - r)R_g + L \downarrow - L \uparrow \tag{20}$$

Fig. 2. Illustration of the trapezoid method used for identifying wet and dry pixels; source: [Fellah et al. 2021]

G is calculated using an empirical approach proposed by Moran et al. [1989]:

$$G = 0.583\exp(-2.13NDVI)R_n \tag{21a}$$

In the case where the NDVI < 0 the formula then becomes:

$$G = 0.583R_n \tag{21b}$$

The parameter φ is determined based on the interpretation of the trapezoid shape of the scatter plot between the surface temperature (T_s) and the vegetation index (NDVI) (Fig. 2) according to Stisen et al. [2008] by the expression:

$$\varphi = \frac{T_s - T_{s\,min}}{T_{s\,max} - T_{s\,min}} (\varphi_{max} - \varphi_{min}) + \varphi_{min} \tag{22}$$

The parameter φ_{min} is deducted according to the fraction cover of canopy (f_c) by:

$$\varphi_{min} = \varphi_{max} f_c \tag{23}$$

where

$$\varphi_{max} = \frac{\Delta + \gamma}{\Delta} \tag{24}$$

and f_c is given by:

$$f_c = \left(\frac{NDVI - NDVI_{min}}{NDVI_{max}\ NDVI_{min}} \right)^2 \tag{25}$$

where: $NDVI_{min}$ = minimal value of normalised difference vegetation index, $NDVI_{max}$ = maximal value of normalised difference vegetation index.

Two-source energy balance (TSEB)

Unlike the single-layer approaches (METRIC and TIM), which use surface temperature as a relative indicator to differentiate dry and wet pixels and interpolate between the two boundaries, TSEB model adopts a more physical approach to interpret the surface temperature in relation to the energy balance [Choi et al. 2009], and separates the Earth's surface into two components: soil surface and vegetation. Surface temperature is partitioned at the zenith angle (θ) in the contributions of the soil and canopy using the equation:

$$T_{rad}(\theta) = \left[f_c(\theta)\ T_c^4 + (1 - f_c(\theta))\ T_{sl}^4 \right]^{\frac{1}{4}} \tag{26}$$

where: T_{rad} = radiative surface temperature, f_c = the fraction cover of the canopy, depending on the leaf area index (LAI) as f_c = 1 – exp (–0.5LAI). Therefore, sensible heat flux H (soil and vegetation) is calculated:

$$H = H_c + H_s \tag{27}$$

$$H_c = \rho\ Cp\frac{T_c - T_{ac}}{r_x} \tag{28}$$

and

$$H_s = \rho\ Cp\frac{T_{sl} - T_{ac}}{r_{sl}} \tag{29}$$

$$H = \rho\ Cp\frac{T_{ac} - T_a}{r_{ah}} \tag{30}$$

where: H_c = canopy sensible heat flux [Kustas, Norman 1999]. Two energy balances are calculated separately for soil and vegetation:

$$R_n = R_{ns} + R_{nc} = H + LE + G \tag{31}$$

$$R_{ns} = H_c + LE_s + G \tag{32}$$

$$R_{nc} = H_c + LE_c \tag{33}$$

where: H_s and H_c = sensible heat fluxes separated between soil and vegetation, R_{ns} and R_{nc} = the net radiation for the soil and vegetation. The canopy latent heat flux (LE_c) is calculated from the Priestley-Taylor equation: (LE_c = 1.26 fg Δ : (Δ + γ) R_{nc}), where: γ = the psychrometric constant, generally equal to 0.066

kPa·K^{-1}. The soil latent heat flux ($LE_s = R_{ns} + G + H_s$) is calculated as a residual of the energy balance, G is calculated using the fraction of the R_{ns} ($G \approx 0.35R_{ns}$) [CHOUDHURY et al. 1987]. TSEB uses meteorological and remote sensing data in order to calculate the soil and vegetation temperatures to finally calculate the surface energy fluxes; however it remains sensitive to the uncertainty of the T_s caused by the quality of the sensors as well as the emissivity errors due to atmospheric correction.

Soil plant atmosphere and remote sensing *ET* (SPARSE)

Articulating on the logic of TSEB model and formulations at the cutting edge of turbulent and radiative exchange, SPARSE model is a two-source model with two versions (serial and parallel) which estimates the evaporation of the soil and the transpiration of the vegetation separately by estimating the components of the energy balance for the soil and the vegetation. At contrary to TSEB, the SPARSE algorithm uses the Penman-Monteith formula rather than that of Priestley-Taylor for the estimation of the potential transpiration applicable in semi-arid zones [COLAIZZI et al. 2012] because of the coefficient 1.26 suggested by Priestley-Taylor underestimates transpiration and overestimates evaporation. SPARSE is a linearisation of all the energy balance equations.

Prescribed mode and retrieval mode

The SPARSE model is based on the same logic of single-layer models such as SEBAL, METRIC and SEBS for the identification of extremely dry and wet sites in a "prescribed" mode in order to provide the theoretical boundaries (stress conditions where sensible heat flux is maximum and potential condition where the latent heat flux is maximum), these two boundaries serve to frame the second "recovery" mode which uses the radiative surface temperature (T_{rad}) to estimate the surface energy fluxes (Fig. 3).

"Layer" series version and "Patch" parallel version

Like two-source energy balance (TSEB), soil plant atmosphere and remote sensing *ET* (SPARSE) offers two versions: "Layer" and "Patch". "Layer" version offers a soil-vegetation couple closely linked with a series resistance system with a single temperature at the aerodynamic level, "Patch" version offers an "atmosphere soil" system independent of the "atmosphere vegetation" system with two aerodynamic temperatures (Fig. 4).

Energy fluxes and surface radiative temperature are expressed for both versions:

$$R_{nsl} = G + H_s + LE_s \tag{34}$$

$$R_{nc} = H_c + LE_c \tag{35}$$

$$H = H_s + H_v \tag{36}$$

$$LE = LE_{sl} + LE_c \tag{37}$$

$$G = x_g R_{ns} \tag{38}$$

Serial version "Layer":

$$H_s = \rho c_p \frac{T_{sl} - T_s}{r_{as}} \tag{39}$$

$$H_c = \rho C_p \frac{T_c - T_s}{r_{av}} \tag{40}$$
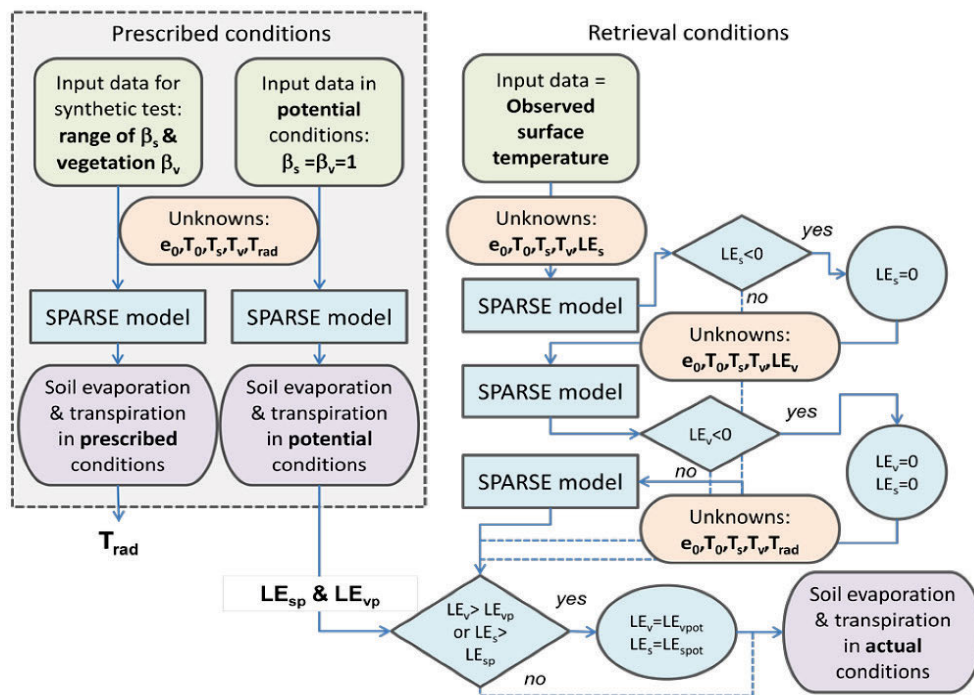
$$H = \rho C_p \frac{T_s - T_a}{r_{ah}} \tag{41}$$

Fig. 3. Flowchart of the SPARSE algorithm under prescribed and recovery conditions; source: [BOULET *et al.* 2015]
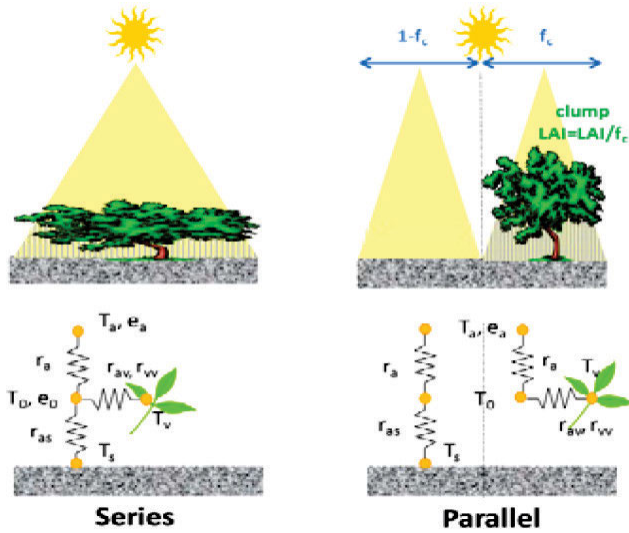
Fig. 4. Diagram showing model approaches in series and in parallel; source: Boulet et al. [2015]

$$LE_s = \frac{\rho\, C_p}{\gamma} \beta_s \frac{e_{\text{sat}}(T_s)\ -\ e_0}{r_{as}\ +\ r_{s\text{smin}}} \tag{42}$$

$$LE_c = \frac{\rho\, C_p}{\gamma} \beta_v \frac{e_{\text{sat}}(T_c)\ -\ e_0}{r_{av}\ +\ r_{vv\text{min}}} \tag{43}$$

$$LE = \frac{\rho\, C_p}{\gamma} \frac{e_0\ -\ e_a}{r_{ah}} \tag{44}$$

Parallel version "Patch":

$$H_s = (1 - f_c)\rho Cp \frac{T_s - T_a}{r_{as} + r_a} \tag{45}$$

$$H_v = f_c \rho Cp \frac{T_v - T_a}{r_{av} + r_a} \tag{46}$$

$$H = \rho Cp \frac{T_0 - T_a}{r_a} \tag{47}$$

$$LE_s = (1 - f_c)\frac{\rho Cp}{\gamma} \beta_s \frac{e_{\text{sat}}(T_s)\ -\ e_a}{r_{as} + r_{s\text{smin}} + r_a} \tag{48}$$

$$LE_v = f_c \frac{\rho Cp}{\gamma} \beta_v \frac{e_{\text{sat}}(T_v)\ -\ e_a}{r_{av}\ +\ r_{vv\text{min}}\ +\ r_a} \tag{49}$$

$$LE = \frac{\rho Cp}{\gamma} \frac{e_0\ -\ e_a}{r_a} \tag{50}$$

Bowen ratio energy balance (BREB)

In this work and for the validation of the data simulated by the four models we calculated the latent heat flux by the energy balance method of the Bowen ratio (BREB) from measurements at two levels (0.5 and 2.5 m above surface) of air temperature using chromel-alumel thermocouples and relative humidity using Vaisala capacitive probes (Model HMP35D). Generally, the BREB method has an uncertainty of ~20% [Kustas, Norman 1999].

$$\beta o = \frac{H}{LE} \cong \frac{\Delta T}{\Delta e} \tag{51}$$

where: ΔT and Δe = temperature and vapour pressure gradient between the two levels of measurements, respectively. We use the calculated Bowen ratio to derive the sensible and latent heat fluxes:

$$H = \frac{\beta o(R_n - G)}{1 + \beta o} \tag{52}$$

$$LE = \frac{(R_n - G)}{1 + \beta o} \tag{53}$$

RESULTS AND DISCUSSION

In this work, the simulation of the energy balance equation by the four models (METRIC, TIM, TSEB and SPARSE) offers us the possibility to demonstrate that the surface parameters, namely albedo, vegetation index and surface temperature, obtained from optical and thermal remote sensing data, allows us to simulate the latent heat flux (*LE*), estimated for METRIC as the residual term of the energy balance equation, estimated for TIM directly using the Priestley-Taylor equation, and estimated for TSEB and SPARSE by calculating the latent heat flux of vegetation (*LE_c*) and soil (*LE_s*) separately. To assess the performance of the results of the four models, two statistical measures were used: the *RMSE* and the *bias* (average difference between the estimated and observed values). For validation of model output results and in the luck of validation mean of *ET* or *LE* at large-scale, the simulated *LE* latent heat flux is not accurate and requires careful consideration [Hamimed et al. 2014]. In our work, we used the Bowen ratio method, 3 values (pixels), for the four days, the first point was characterised by dense vegetation, the second by moderate vegetation, the third by bare soil, measured on the ground for the latent heat flux. These values were compared with those obtained from the four models, noting that this type of validation does not ensure that the model provides reliable flux across all surface types [Choi et al. 2009; Khaldi et al. 2011].

SURFACE TEMPERATURE

The surface temperature (*T_s*) has a major influence on the estimation of the latent heat flux (*LE*) to which they are linked by the equation of the surface energy balance. It is essential to acquire the information on soil moisture needed in several areas including a large-scale irrigation project (mass agriculture). The correlation between the surface temperature (*T_s*) of the (Landsat 8 OLI/TIRS) satellite and that measured on the ground, obtained by an Apogee infrared radiometer (IRTS-P), showed reliable results with a correlation coefficient (R^2) of 0.96. Simulated surface temperature T_s is slightly underestimated relative to the measured surface temperature, with *RMSE* of 3.45 K and a bias of –3.36 K (Fig. 5).

Temperature errors recorded are almost identical to the values reported in previous studies with an RMSE ranging from approximately 2.8 to 4.2 K [Consoli, Vanella et al. 2014; Fellah et al. 2021; Madugundu et al. 2017; dos Santos et al. 2020; Timmermans et al. 2007; Zou et al. 2018]. Noting that for our study site, surface temperature Ts and bare soils (dry pixels) are
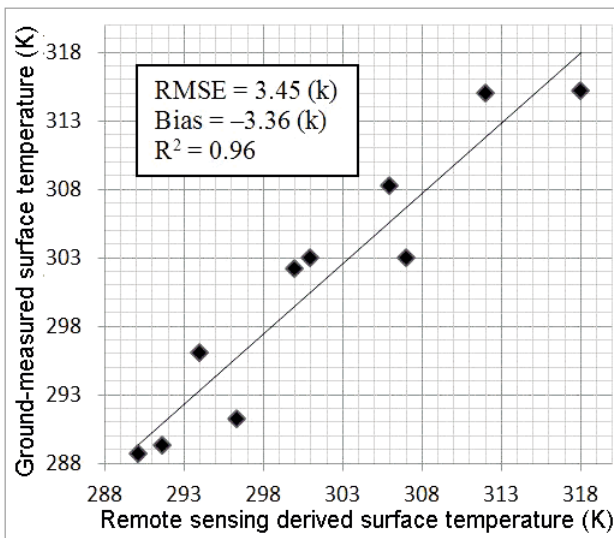
Fig. 5. Comparison between ground-measured and simulated surface temperature on September 1, 2014 (DOY 244); *RMSE* = root-mean-square error; *bias* = average difference between the estimated and observed values, R^2 = correlation coefficient; source: own study

characterised by high values, while for dense vegetation of irrigated soils (wet pixels) are characterised by low values (Tab. 4).

NET RADIATION

The spatialisation of net radiation R_n with the four models showed a significant agreement with a slight overestimation for TSEB and SPARSE, the difference is probably due to the different formulation between the two single-source models (METRIC and TIM) which directly estimate net R_n radiation using the formula by ALLEN *et al.* [1998], and the two-source TSEB and SPARSE models, which estimate the soil net radiation R_{ns} and vegetation net radiation R_{nc}, separately and finally deduct the R_n value as the sum of the two fluxes. It is noted that higher values of net radiation are simulated over a dense and generally moist canopy (high *NDVI* and low T_s) (Tab. 5).

SOIL HEAT FLUX

Conductive soil heat flux (*G*) estimated by TSEB and SPARSE showed a significant overestimation compared to METRIC and TIM especially for the two days, DOY 356 and DOY 071, which are characterised by a low surface temperature with RMSE up to 97 and 70 W·m^{-2} between METRIC and TSEB. This significant difference comes from the formulation of TSEB and SPARSE which estimates *G* as a fraction of R_{ns} with an x_g coefficient of 0.35 for TSEB, and 0.4 for SPARSE, as for METRIC and TIM, *G* is a fraction of R_n. However, for the days with a high surface temperature T_s, the *RMSE* decreases to 6.57. The comparison between the measured soil heat flux values and those simulated by remote sensing data shows that the METRIC and TIM models lead to an underestimation of *G* with *RMSE* of 21.3 W·m^{-2} and a *bias* of –20.8 W·m^{-2}, while the TSEB and SPARSE models lead to an overestimation with *RMSE* of 11.9 W·m^{-2} with a *bias* of 10.7 W·m^{-2}. These results are very similar to the results of previous studies: TEIXEIRA *et al.* [2009] with *RMSE* of 13.3 W·m^{-2}, MKHWANAZI *et al.* [2012] with *RMSE* of 14.2 W·m^{-2}, HAMIMED *et al.* [2014] with *RMSE* of 13.2 W·m^{-2}, NEHAL *et al.* [2017] with *RMSE* of 14 W·m^{-2}, FELLAH *et al.* [2021] with *RMSE* of 15.2 W·m^{-2}. It is also noted that for hot and dry surfaces the values of *G* are higher, ranging up to 93 W·m^{-2} for the METRIC and TIM models, and more than 135 W·m^{-2} for the TSEB and SPARSE models, however, *G* values remain lower for canopies and cold surfaces (Tab. 5). The impact of soil heat flow *G* on available energy (R_n – *G*) remains low, which means that model inaccuracies do not have an impact on energy balance modelling and everything on the latent heat flux (*LE*) [NEHAL *et al.* 2017].

SENSIBLE HEAT FLUX

The spatialisation of the sensible heat flux (*H*) is the most delicate point for the residual models because it allows the estimation of the latent heat flux due to difficulties in estimating the aerodynamic resistance to heat transfer (r_{ah}) except for the contextual model TIM which estimates *LE* directly without estimating *H*, and estimates it as a residual term by closing the

Table 4. Instantaneous average values of surface parameters above dry and wet pixels in study area

Parameter	Unit	01.09.2014 (DOY 244)		19.10.2014 (DOY 292)		22.12.2014 (DOY 356)		12.03.2015 (DOY 071)	
		dry pixel	wet pixel	dry pixel	wet pixel	dry pixel	wet pixel	dry pixel	wet pixel
NDVI		0.08	0.70	0.9	0.73	0.12	0.75	0.11	0.79
Albedo	–	0.32	0.21	0.29	0.16	0.20	0.15	0.27	0.21
Emissivity		0.92	0.99	0.91	0.99	0.90	0.99	0.91	0.99
Surface temperature	K	334.1	307.3	325.6	297.4	298.9	283.4	329.6	303.5
Near-surface air temperature difference	K	2.34	0	2.22	0	2.42	0	3.51	0
Friction velocity	s·m^{-1}	0.30	0.37	0.26	0.29	0.25	0.28	0.35	0.42
Monin-Obukhov length	m	–34.1	–825.6	–13.8	–769.4	–10.9	–730.2	–13.8	390.1
Aerodynamic resistance to heat transport	s·m^{-1}	20.5	17.3	19.1	16.6	22.4	26.1	15.3	18.1

Source: own study.

Table 5. Comparison of the net radiation (R_n), soil heat flux (G), sensible heat flux (H) and latent heat flux (LE) obtained from the four models: mapping evapotranspiration at high resolution with internalised calibration (METRIC), trapezoid interpolation model (TIM), two-source energy balance (TSEB), soil plant atmosphere and remote sensing evapotranspiration (SPARSE)

| Model	Pixel	01.09.2014 (DOY 244)				19.10.2014 (DOY 292)				22.12.2014 (DOY 356)				12.03.2015 (DOY 071)			
		R_n	G	H	LE	R_n	G	H	LE	R_n	G	H	LE	R_n	G	H	LE
METRIC	dry	163	93	271	0.11	193	62	466	7.13	148	22	157	7.62	261	74	348	14
TIM		163	93	359	0.13	193	62	322	5.18	148	22	197	11.6	261	74	379	12
TSEB		166	111	296	2.64	193	104	95	118	198	136	59	88.7	316	135	117	216
SPARSE		181	121	299	1.7	210	111	70	133	164	72	17	123	276	129	82	186
METRIC	wet	605	35	0	548	634	31	0	475	425	4	0	325	626	22	0	582
TIM		605	35	0	577	634	31	0	477	425	4	–73	374	626	22	–16	582
TSEB		647	42	–16	596	532	38	–76	501	392	69	–28	282	681	62	–27	568
SPARSE		641	–3	–21	549	553	42	–30	471	361	33	–4	293	647	55	–13	528
METRIC	average	421	85	172	164	387	56	209	120	271	16	54	200	518	51	106	360
TIM		421	85	211	125	387	56	137	192	271	16	27	226	518	52	68	397
TSEB		436	101	142	192	395	77	24	294	328	113	13	201	584	115	23	445
SPARSE		446	84	137	225	411	82	25	304	294	58	6	229	545	109	24	413

Source: own study.

Currently, dry and warm bare soils (low $NDVI$ values and high T_s values) are characterised by low R_n values. The validation of the R_n results showed that the ground-measured values and the remotely sensed-obtained (by all models) showed a better agreement with $RMSE$ of 27.6 W·m^{-2} for METRIC and TIM, and about 32.4 W·m^{-2} for TSEB and SPARSE. These values are consistent with previous studies [CHOI et al. 2009; FELLAH et al. 2021; DOS SANTOS et al. 2020; TANG, LI 2015; ZOU et al. 2018].

energy balance equation. The r_{ah} is low for hot and dry pixels (bare soil) (Tab. 4), which causes the release of heat into the atmosphere due to the large differences between surface (T_s) and air (T_a) temperatures. However, for wet pixels (irrigated area), r_{ah} values are also low because the available energy (R_n – G) is transformed into ET. This difference in sensible heat flux for dry and wet pixels is caused by the soil moisture condition and its impact on the energy distribution between latent and sensible heat flux. Wet surfaces are characterised by low H values while dry surfaces are characterised by high H values (Tab. 5).

Sensible heat flux values simulated by METRIC and TIM are overestimated compared to that measured in soil with $RMSE$ values ranging from 35 to 85 W·m^{-2} for METRIC, and from 80 to 125 W·m^{-2} for TIM. It was noted that the two-source models are more accurate for estimating H with $RMSE$ between 30 and 75 W·m^{-2} for TSEB and between 25 and 60 W·m^{-2} for SPARSE. Errors in the estimates are almost identical to those in previous studies [DOS SANTOS et al. 2020; FELLAH et al. 2021; KUSTAS, NORMAN 1999; TANG, LI 2015; TIMMERMANS et al. 2007]. These results are explained by the type of formulation used in each model, thus the two-source models are more robust than the single-source models which do not take into account all resistance parameters such as stomatic resistance and which use a single surface temperature, while the two-source models use a temperature for soil T_{sl} and vegetation T_c for estimation H_c and H_s.

H varies in a range from $H = 0$ (extremely wet pixel) to $H = R_n$ – G (extremely dry pixel), the histograms of H are produced almost similarly by METRIC and TIM covering a full range from 0 to 410 W·m^{-2} (Fig. 6) on average. To reinforce the interpolation of values in this range, there is also a homogeneous spatial distribution of H on the ground with extreme values for

dry bare soil at high surface temperature, and near zero for wet dense vegetation at low surface temperature. However, the problem is that when both limits (dry and wet) do not exist, the two single-source models, METRIC, and especially, TIM, seem to struggle to simulate the sensible heat flux H because they are sensitive to the temperature difference between the two dry and wet limits. In order to correct this problem, we calculated theoretically the four temperatures of the four points (dry bare soil, wet bare soil, dense wet vegetation and dense dry vegetation)
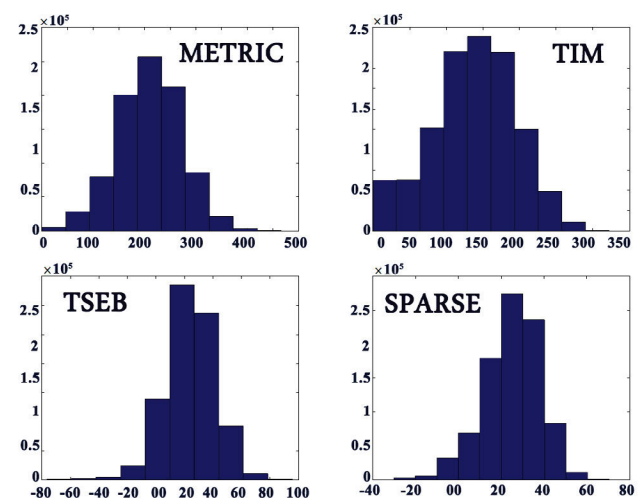
Fig. 6. Sensible heat flux (H, W·m^{-2}) frequency histograms from mapping evapotranspiration at high resolution with internalised calibration (METRIC) model, trapezoid interpolation model (TIM), two-source energy balance (TSEB) model, soil plant atmosphere and remote sensing evapotranspiration (SPARSE) models for 19.10.2014 (DOY 292); source: own study

for days DOY 356 (22.12.2014) and DOY 71 (12.03.2015), two days when the temperature difference is minimal, to reduce estimation errors of H, but despite this, these two models have difficulties in simulating H. The TSEB and SPARSE models estimate H by calculating different aerodynamic resistances and stomatic resistance, and do not make any hypothesis on hydrological and temperature parameters, that is to say, the existence of extremely dry and wet sites, we thus notice a frequency distribution of H which culminates at lower limited values and in a narrow range, between 100 and 200 W·m^{-2}. These results are almost identical to those obtained in previous studies [Choi *et al.* 2009; French *et al.* 2005; Timmermans *et al.* 2007] which found a similar restriction of the flux range using SEBAL compared to TSEB, and TIM–METRIC compared to TSEB.

LATENT HEAT FLUX

In the absence of a means for validation of the latent heat flux (LE) at large-scale, the simulated results are not accurate and require careful consideration [Hamimed *et al.* 2014]. The method used for validation is the Bowen ration which is based on the comparison of the LE ground-measured values (3 values for the four days: the first point characterised by dense vegetation, the second by moderate vegetation, the third by bare soil) with those obtained from the four models. This statistics comparison (*bias* and *RMSE*) shows a difference illustrated in (Tab. 6).

These statistics are consistent with those obtained by the other researchers [Choi *et al.* 2009; dos Santos *et al.* 2020; Timmermans *et al.* 2007]. The result of the comparison of the simulated LE with the ground measured LE shows that the four models provide comparable outputs (Fig. 7) with a slight advantage of the METRIC model in case of large temperature and humidity differences, which means the existence of extremely dry, hot and extremely wet and cold sites, this model can be considered as a promising approach for the spatialisation of ET in the case of places where the means of validation and information are inaccessible.

However, on days when the difference in temperature and humidity is non-existent (cold winter days), the single-source models, METRIC and, especially, TIM, struggle to simulate the sensible and latent heat flux (Tab. 6), whereas the two-source models TSEB and SPARSE are more accurate because of their algorithms, which use two temperatures (vegetation T_c and soil T_{sl}) to estimate pixel-by-pixel flux and do not assume the existence of extremely dry and wet sites. The SPARSE model is the most accurate for these conditions and in second position is TSEB model. The LE varies for the 4 models and for the 4 dates according to the averages represented in Table 6, the inter-comparison of the LE between the models is represented in Figures 8–11.

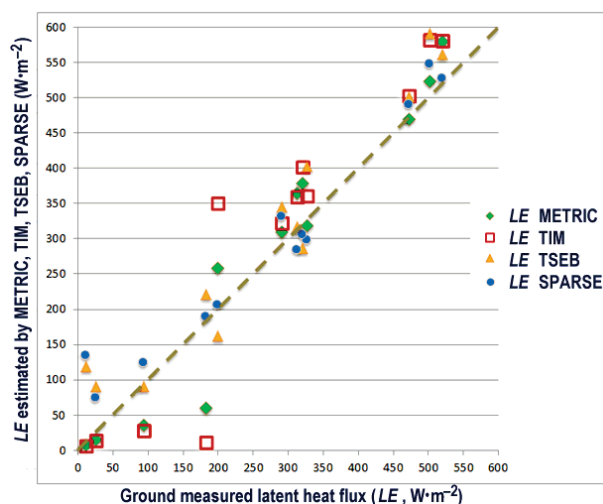The spatial distributions of the latent heat fluxes between the four models showed a significant agreement (Fig. 12).

Fig. 7. Comparison between the latent heat flux (LE) measured on the ground and the latent heat flux estimated by the four models for the three points for the four days (01.09.2014 – DOY 244, 19.10.2014 – DOY 292, 22.12.2014 – DOY 356, 12.03.2015 – DOY 071); METRIC, TIM, TSEB, SPARSE as in Tab. 5; source: own study

Table 6. Statistics comparing latent heat flux (LE) between field measurements and values obtained by the four models

| DOY	Observed *LE* (Bowen)		*LE* (METRIC)			*LE* (TIM)			*LE* (TSEB)			*LE* (SPARSE)		
			average	*RMSE*	*bias*	average	*RMSE*	*bias*	average	*RMSE*	*bias*	average	*RMSE*	*bias*
244	wet pixel	502	523	21	–21	582	80	–80	591	89	–89	547	45	–45
	moderate pixel	327	318	9	9	361	34	–34	403	76	–76	298	29	29
	dry pixel	26	16	10	10	14	12	12	90	64	–64	73	47	–47
292	wet pixel	472	469	3	3	503	31	–31	501	29	–29	490	18	–18
	moderate pixel	291	310	19	–19	322	31	–31	345	54	–54	331	41	–41
	dry pixel	11	7	4	4	6	5	5	119	108	–108	135	124	–124
356	wet pixel	320	378	58	–58	401	81	–81	287	34	34	305	15	15
	moderate pixel	199	259	60	60	350	151	–151	162	27	27	207	8	–8
	dry pixel	94	35	59	59	29	65	–65	90	4	4	125	31	–31
071	wet pixel	520	579	59	–59	581	61	–61	561	41	–41	527	7	–7
	moderate pixel	313	364	51	–51	359	46	–46	317	5	–5	284	29	29
	dry pixel	182	59	123	123	12	170	170	220	38	–38	190	08	–08

Explanations: DOY, RMSE, bias, METRIC, TIM, TSEB, SPARSE as in Fig. 5, Tab. 5.
Source: own study.
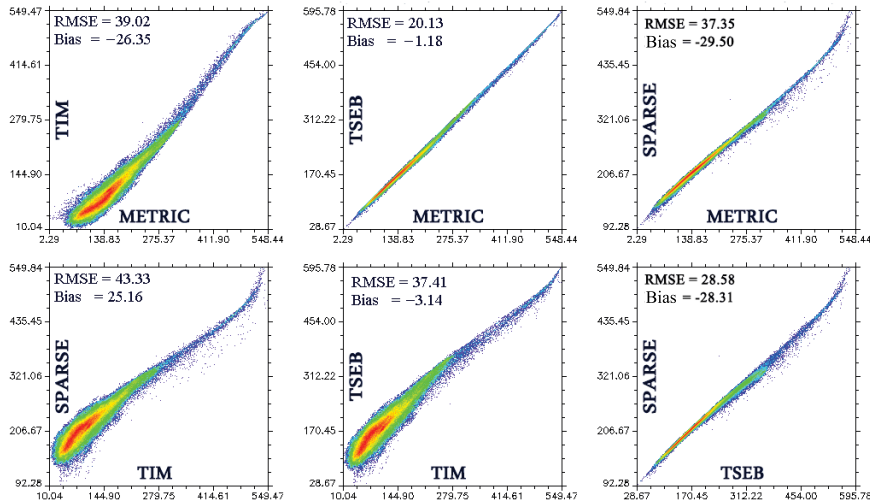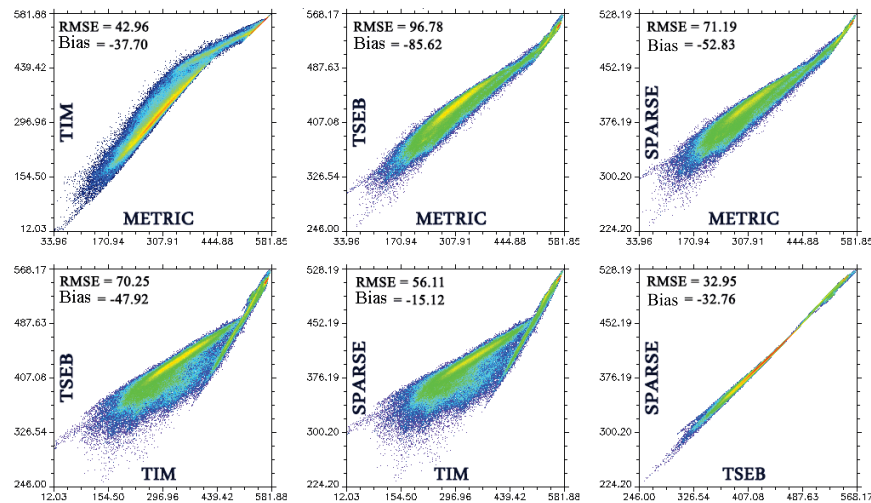
Fig. 8. Density plots of latent heat flux *LE* (W·m⁻²) for METRIC–TIM, METRIC–TSEB, METRIC–SPARSE, TIM–TSEB, TIM–SPARSE and TSEB–SPARSE of the day 01.09.2014 (DOY 244); METRIC, TIM, TSEB, SPARSE as in Tab. 5; source: own study
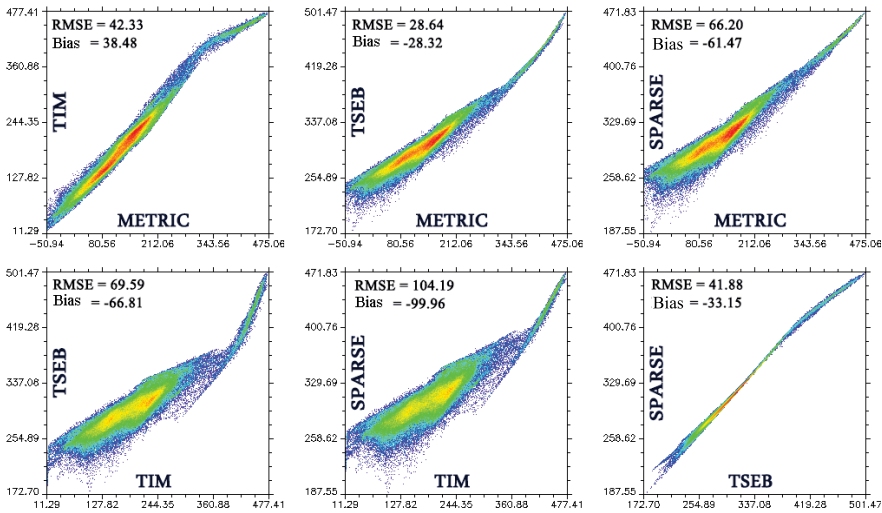

Fig. 9. Density plots of latent heat flux *LE* (W·m⁻²) for METRIC–TIM, METRIC–TSEB, METRIC–SPARSE, TIM–TSEB, TIM–SPARSE and TSEB–SPARSE of the day 19.10.2014 (DOY 292); METRIC, TIM, TSEB, SPARSE as in Tab. 5; source: own study
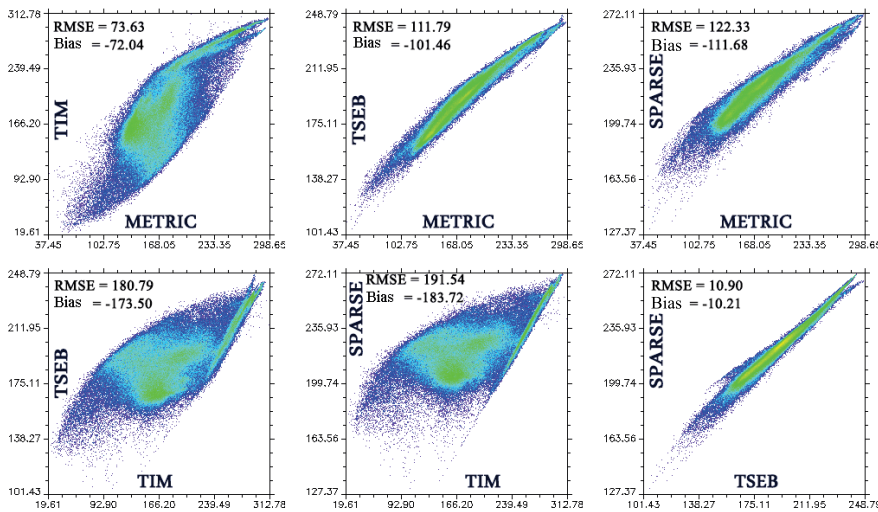
Fig. 10. Density plots of latent heat flux *LE* (W·m⁻²) for METRIC–TIM, METRIC–TSEB, METRIC–SPARSE, TIM–TSEB, TIM–SPARSE and TSEB–SPARSE of the day 22.12.2014 (DOY 356); METRIC, TIM, TSEB, SPARSE as in Tab. 5; source: own study

Fig. 11. Density plots of latent heat flux *LE* (W·m⁻²) for METRIC–TIM, METRIC–TSEB, METRIC–SPARSE, TIM–TSEB, TIM–SPARSE and TSEB–SPARSE of the day 12.03.2015 (DOY 071); METRIC, TIM, TSEB, SPARSE as in Tab. 5; source: own study
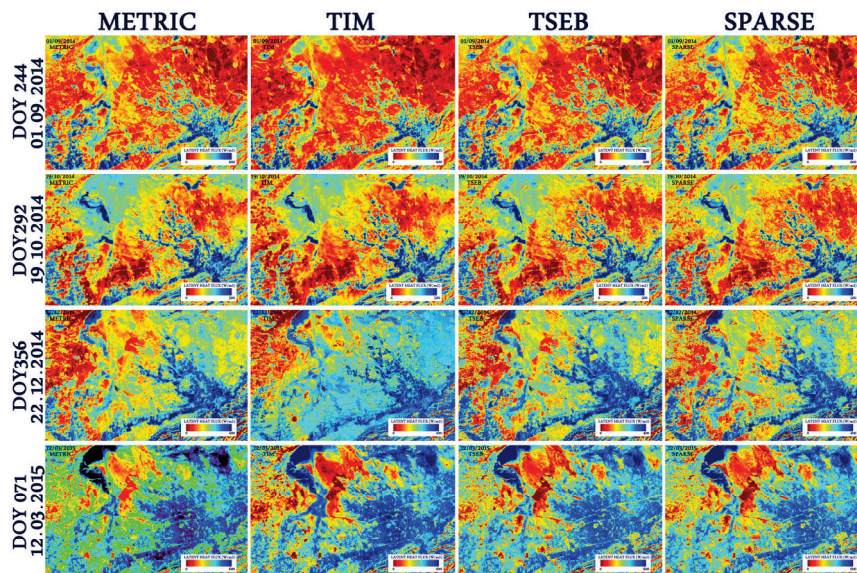
Fig. 12. Spatial distributions of the latent heat fluxes estimated with METRIC, TIM, TSEB, SPARSE for the four days (01.09.2014, 19.10.2014, 22.12.2014, 12.03.2015); METRIC, TIM, TSEB, SPARSE as in Tab. 5; source: own study
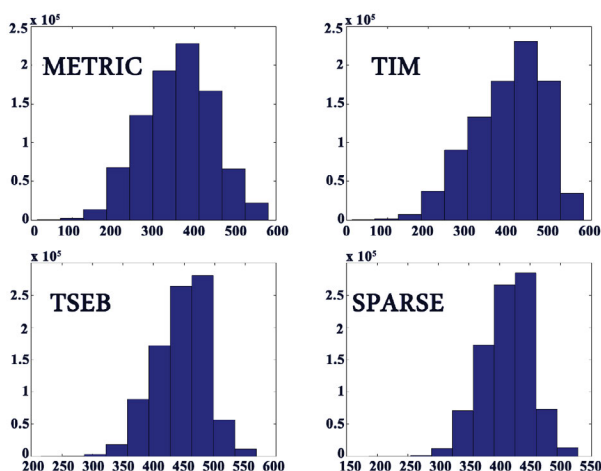
Fig. 13. Latent heat flux (*LE*, W·m⁻²) frequency histograms from METRIC, TIM, TSEB, SPARSE for 12.03.2015 (DOY 071); METRIC, TIM, TSEB, SPARSE as in Tab. 5; source: own study

Despite the difference for *G* and *H* between the two models METRIC–TIM and TSEB–SPASRE, the first two overestimate *H* and underestimate *G*, while the last two overestimate *G* and underestimate *H*, so in the end they give almost the same results on the days when there is a big difference in temperature and humidity, DOY 244 and DOY 292. The days when there is a small difference, DOY 71 or practically DOY 356, METRIC and especially TIM have difficulties to simulate *LE*, which makes the difference significant with the TSEB and SPARSE models which are very robust in these conditions, noting that the SPARSE is the best in these conditions. It is also noted that TIM and METRIC produce *LE* histograms, covering a full range from 0 to 600 W·m⁻² forcing interpolation of *LE* values across this range applying the hypothesis of existence of extremely wet sites $L = R_n - G$ and dry $LE = 0$. TSEB and SPARSE produce the highest *LE* values covering a narrow range of 200 to 550 W·m⁻² (Fig. 13), with an estimated latent heat flux pixel by pixel independently of the others assuming there are no assumptions about the scope of the image.

CONCLUSIONS

In this work, we have shown the value of multi-spectral satellite data with a high spatial resolution (Landsat 8 OLI/TIRS) to estimate energy flux and in particular, the latent heat flux which is the energy equivalent of *ET* and the water state. For our study site, which is characterised by heterogeneous soil cover and during days when there is a large difference in temperature and soil moisture, the four models used provide almost similar *LE* outputs with a slight advantage of the METRIC model with *RMSE* between 9 and 21 W·m^{-2} for DOY 244, on the other hand on days when this difference is small, the two-source models, TSEB and SPARSE, distinguish and offer us a simulation close to reality with an RMSE between 8 and 15 W·m^{-2} for DOY 071, unlike one-source models, METRIC and TIM, have difficulties in simulating latent heat flux. The METRIC and TIM models force the interpolation of *H* and *LE* which is reflected in histograms with a wide distribution, unlike TSEB and SPARSE. The greatest differences between the models for *H* and *LE* were identified in the sites where the vegetation cover was split with a leaf area index (*LAI*) < 2. Underestimation of *G* and overestimation of *H* for METRIC and TIM, and overestimation of *G* and under-estimation of *H* for TSEB and SPARSE, tended to modulate the deviation in *LE* towards the end for the four models. Although comparisons with ground measurements of the *LE* using the Bowen ratio method with the four models gave satisfactory and encouraging results for the future, two models stand out in this study, METRIC and SPARSE, the first performing in summer and autumn (large difference in temperature and soil moisture on the site), and the second performing in winter and spring (small difference in temperature and soil moisture on the site). This wide study site with its heterogeneous coverage allowed us to test the four models, something that was not tested in previous studies with generally homogeneous sites with a simple area like the site of soil moisture–atmosphere coupling experiment (SMACEX). In perspective, since the two models have distinguished themselves from the others, METRIC and SPARSE, respectively with their strengths and weakness, we propose a hybrid methodology that is based on the logic of the METRIC model in the conditions of large temperature and humidity differences, which is the case in summer and autumn days with a partially vegetated cover, and the SPARSE logic, based on the two-source pixel-by-pixel method in the conditions of low temperature and humidity difference in the image, which applies to winter and spring days with an almost total natural cover (no dry bare soil). Until technology gives us the opportunity to have daily high-resolution images, drones are very useful, especially in extreme weather conditions with a resolution per millimetre, but the only disadvantage remains the limit of the computer means of processing large amounts of data.

ACKNOWLEDGEMENTS

REFERENCES

ALLEN R.G., PEREIRA L.S., RAES D. SMITH M. 1998. Crop evapotranspiration – guidelines for computing crop water requirements. FAO Irrigation and Drainage Paper. No. 56. Rome. FAO. ISBN 92-5-104219-5 pp. 300.

ALLEN R.G., TASUMI M., TREZZA R. 2007. Satellite-based energy balance for mapping evapotranspiration with internalized calibration (METRIC) – model. Journal of Irrigation and Drainage Engineering. Vol. 133(4) p. 380–394. DOI 10.1061/(ASCE)0733-9437(2007)133:4(380).

BARSI J.A., SCHOTT J.R., PALLUCONI F.D., HOOK S.J. 2005. Validation of a web-based atmospheric correction tool for single thermal band instruments. Earth Observing Systems X. Proceedings of Society of Photo-Optical Instrumentation Engineers (SPIE). Vol. 5882. p. 136–142. DOI 10.1117/12.619990.

BASTIAANSSEN W.G.M. 2000. SEBAL-based sensible and latent heat fluxes in the irrigated Gediz Basin, Turkey. Journal of Hydrology. Vol. 229(1–2) p. 87–100. DOI 10.1016/S0022-1694(99)00202-4.

BASTIAANSSEN W.G.M., MENENTI M., FEDDES R.A., HOLTSLAG A.A.M. 1998. Remote sensing surface energy balance algorithm for land (SEBAL), 1. Formulation. Journal of Hydrology. Vol. 212–213(1–4) p. 198–212. DOI 10.1016/S0022-1694(98)00253-4.

BENZATER B., ELOUISSI A., BENARICHA B., HABI M. 2019. Spatio-temporal trends in daily maximum rainfall in northwestern Algeria (Macta watershed case, Algeria). Arabian Journal of Geosciences. Vol. 12 (370) p. 1–18. DOI 10.1007/s12517-019-4488-8.

BERK A., ANDERSON G.P., BERNSTEIN L.S., ACHARYA P.K., DOTHE H., MATTHEW M.W., ..., HOKE M.L. 1999. MODTRAN4 radiative transfer modeling for atmospheric correction. Optical spectroscopic techniques and instrumentation for atmospheric and space research III. Proceedings of Society of Photo-Optical Instrumentation Engineers. SPIE's International Symposium on Optical Science, Engineering, and Instrumentation. Vol. 3756 p. 348–353. DOI 10.1117/12.366388.

BOULET G., MOUGENOT B., LHOMME J.P., FANISE P., LILI-CHABAANE Z., OLIOSO A., ..., LAGOUARDE J.P. 2015. The SPARSE model for the prediction of water stress and evapotranspiration components from thermal infra-red data and its evaluation over irrigated and rainfed wheat. Hydrology and Earth System Sciences. Vol. 19(11) p. 4653–4672. DOI 10.5194/hess-19-4653-2015.

BRUTSAERT W. 1982. Evaporation into the atmosphere: Theory, history and applications. Springer Dordrecht. ISBN 978-90-277-1247-9 pp. 299. DOI 10.1007/978-94-017-1497-6.

CHANDER G., MARKHAM B.L., HELDER D.L. 2009. Summary of current radiometric calibration coefficients for Landsat MSS, TM, ETM+, and EO-1 ALI sensors. Remote Sensing of Environment. Vol. 113 (5) p. 893–903. DOI 10.1016/j.rse.2009.01.007.

CHEHBOUNI A., ESCADAFAL R., DUCHEMIN B., BOULET G., SIMONNEAUX V., DEDIEU G., ..., SOBRINO J.A. 2008. An integrated modelling and remote sensing approach for hydrological study in arid and semi-arid regions: The SUDMED Programme. International Journal of Remote Sensing. Vol. 29(17–18) p. 5161–5181. DOI 10.1080/01431160802036417.

CHIROUZE J., BOULET G., JARLAN L., FIEUZAL R., RODRIGUEZ J.C., EZZAHAR, J., ..., CHEHBOUNI G. 2014. Intercomparison of four remote-sensing-based energy balance methods to retrieve surface evapotranspiration and water stress of irrigated fields in semi-arid climate. Hydrology and Earth System Sciences. Vol. 18(3) p. 1165–1188. DOI 10.5194/hess-18-1165-2014.

CHOI M., KUSTAS W.P., ANDERSON M.C., ALLEN R.G., LI F., KJAERSGAARD J.H. 2009. An intercomparison of three remote sensing-based surface energy balance algorithms over a corn and soybean

production region (Iowa, U.S.) during SMACEX. Agricultural and Forest Meteorology. Vol. 149(12) p. 2082–2097. DOI 10.1016/j.agrformet.2009.07.002.

CHOUDHURY B.J., IDSO S.B., REGINATO R.J. 1987. Analysis of an empirical model for soil heat flux under a growing wheat crop for estimating evaporation by an infrared-temperature based energy balance equation. Agricultural and Forest Meteorology. Vol. 39 (4) p. 283–297. DOI 10.1016/0168-1923(87)90021-9.

COLAIZZI P.D., KUSTAS W.P., ANDERSON M.C., AGAM N., TOLK J.A., EVETT S.R., HOWELL T.A., GOWDA P.H., O'SHAUGHNESSY S.A. 2012. Two-source energy balance model estimates of evapotranspiration using component and composite surface temperatures. Advances in Water Resources. Vol. 50 p. 134–151. DOI 10.1016/j.advwatres.2012.06.004.

CONSOLI S., VANELLA D. 2014. Comparisons of satellite-based models for estimating evapotranspiration fluxes. Journal of Hydrology. Vol. 513 p. 475–489. DOI 10.1016/j.jhydrol.2014.03.071.

CRAGO R.D., BRUTSAERT W. 1992. A comparison of several evaporation equations. Water Resources Research. Vol. 28(3) p. 951–954. DOI 10.1029/91WR03149.

DOS SANTOS C.A.C., MARIANO D.A., NASCIMENTO F.C.A., DANTAS F.R.C., OLIVEIRA G., SILVA M.T., …, NEALE C.M.U. 2020. Spatio-temporal patterns of energy exchange and evapotranspiration during an intense drought for drylands in Brazil. International Journal of Applied Earth Observation and Geoinformation. Vol. 85, 101982 p. 1–11. DOI 10.1016/j.jag.2019.101982.

ELOUISSI A., HABI M., BENARICHA B., BOUALEM S.A. 2017. Climate change impact on rainfall spatio-temporal variability (Macta watershed case, Algeria). Arabian Journal of Geosciences. Vol. 10(22), 496 p. 1–14. DOI 10.1007/s12517-017-3264-x.

FELLAH S., HAMIMED A., MILOUDI K., KHALDI A., BENSLIMANE M., TEIXEIRA A.H.D. 2021. Application of SEBAL and T_s/VI trapezoid models for estimating actual evapotranspiration in the Algerian semi-arid environment to improve agricultural water management. Revista Brasileira de Meteorologia. Vol. 36(2) p. 219–236. DOI 10.1590/0102-77863610020.

FRENCH A.N., JACOB F., ANDERSON M.C., KUSTAS W.P., TIMMERMANS W., GIESKE A., …, BRUNSELL N. 2005. Surface energy fluxes with the Advanced Spaceborne Thermal Emission and Reflection radio-meter (ASTER) at the Iowa 2002 SMACEX site (USA). Remote Sensing of Environment. Vol. 99(1–2) p. 55–65. DOI 10.1016/j.rse.2005.05.015.

GENTINE P., ENTEKHABI D., POLCHER J. 2011. The diurnal behavior of evaporative fraction in the soil-vegetation-atmospheric boundary layer continuum. Journal of Hydrometeorology. Vol. 12(6) p. 1530–1546.

HAMIMED A., KHALDI A., MEHOR M., SEDDINI A. 2009. Estimation of daily actual evapotranspiration in Algerian semiarid environment with satellite ASTER. EARSeL eProceedings. Vol. 8(2) p. 140–151.

HAMIMED A., NEHAL L., KHALDI A., AZZAZ H. 2014. Contribution à la spatialisation de l'évapotranspiration d'un agro-système semi-aride en Algérie par utilisation de la télédétection et du modele METRIC [Contribution to the spatialization of evapotranspiration in a semi-arid agro-system in Algeria using remote sensing and METRIC model]. Physio-Géo – Géographie Physique et Environnement. Vol. 8 p. 197–213. DOI 10.4000/physio-geo.4063.

JIANG L., ISLAM S. 2001. Estimation of surface evaporation map over southern Great Plains using remote sensing data. Water Resources Research. Vol. 37(2) p. 329–340. DOI 10.1029/2000WR900255.

KAUFMAN Y.J., TANRÉ D., REMER L.A., VERMOTE E.F., CHU A., HOLBEN B.N. 1997. Operational remote sensing of tropospheric aerosol over land from EOS moderate resolution imaging spectroradiometer. Journal of Geophysical Research: Atmospheres. Vol. 102(D14) p. 17051–17067. DOI 10.1029/96JD03988.

KHALDI A., HAMIMED A., MEDERBAL K. SEDDINI A. 2011. Obtaining evapotranspiration and surface energy fluxes with remotely sensed data to improve agricultural water management. African Journal of Food Agriculture Nutrition and Development. Vol. 11 (1) p. 4558–4581. DOI 10.4314/ajfand.v11i1.65881.

KUSTAS W.P., DAUGHTRY C.S. 1990. Estimation of the soil heat flux/net radiation ratio from spectral data. Agricultural and Forest Meteorology. Vol. 49(3) p. 205–223. DOI 10.1016/0168-1923 (90)90033-3.

KUSTAS W.P., NORMAN J.M. 1999. Evaluation of soil and vegetation heat flux predictions using a simple two-source model with radio-metric temperatures for partial canopy cover. Agricultural and Forest Meteorology. Vol. 94(1) p. 13–29. DOI 10.1016/S0168-1923(99)00005-2.

LIANG S., SHUEY C., RUSS A., FANG H., CHEN M., WALTHALL C., DAUGHTRY C., HUNT B. 2002. Narrowband to broadband conversions of land surface albedo: II. Validation. Remote Sensing of Environment. Vol. 84(1) p. 25–41. DOI 10.1016/S0034-4257(02)00068-8.

MADUGUNDU R., AL-GAADI K.A., TOLA E., HASSABALLA A.A., PATIL V.C. 2017. Performance of the METRIC model in estimating evapotranspiration fluxes over an irrigated field in Saudi Arabia using Landsat-8 images. Hydrology and Earth System Sciences. Vol. 21(12) p. 6135–6151. DOI 10.5194/hess-21-6135-2017.

MKHWANAZI M., CHÁVEZ J.L., RAMBIKUR E.H. 2012. Comparison of large aperture scintillometer and satellite-based energy balance models in sensible heat flux and crop evapotranspiration determination. International Journal of Remote Sensing Applications. Vol. 2(1) p. 24–30.

MORAN M.S., JACKSON R.D., RAYMOND L.H., GAY L. W., SLATER P.N. 1989. Mapping surface energy balance components by combining Landsat Thematic Mapper and ground-based meteorological data. Remote Sensing of Environment. Vol. 30(1) p. 77–87.

MUZYLEV E.L., USPENSKII A.B., STARTSEVA Z.P., VOLKOVA E.V., KUKHARSKII A.V. 2010. Modeling water and heat balance components for the river basin using remote sensing data on underlying surface characteristics. Russian Meteorology and Hydrology. Vol. 35 p. 225–235. DOI 10.3103/S1068373910030106.

NEHAL L., HAMIMED H., KHALDI A., SOUIDI, Z., ZAAGANE M. 2017. Evapotranspiration and surface energy fluxes estimation using the Landsat-7 enhanced thematic mapper plus image over a semiarid agrosystem in the north-west of Algeria. Revista Brasileira de Meteorologia. Vol. 32 p. 691–702. DOI 10.1590/0102-7786324016.

OLIOSO A., JACOB F. 2002. Estimation de l'évapotranspiration à partir de mesures de télédétection [Evapotranspiration estimation using remote sensing data]. La Houille Blanche. Vol. 88(1) p. 62–67. DOI 10.1051/lhb/2002008.

OLIOSO A., CHAUKI H., COURAULT D., WIGNERON J.P. 1999. Estimation of evapotranspiration and photosynthesis by assimilation of remote sensing data into SVAT models. Remote Sensing of Environment. Vol. 68 p. 341–356.

PAULSON C.A. 1970. The mathematical representation of wind speed and temperature profiles in the unstable atmospheric surface layer. Journal of Applied Meteorology. Vol. 9(6) p. 857–861.

SEGUIN B., ITIER B. 1983. Using midday surface temperature to estimate daily evaporation from satellite thermal IR data. International Journal of Remote Sensing. Vol. 4(2) p. 371–383. DOI 10.1080/01431168308948554.

STAENZ K., SECKER J., GAO B.C., DAVIS C., NADEAU C. 2002. Radiative transfer codes applied to hyperspectral data for the retrieval of

surface reflectance. ISPRS Journal of Photogrammetry and Remote Sensing. Vol. 57(3) p. 194–203. DOI 10.1016/S0924-2716(02)00121-1.

Stisen S., Sandholt I., Nørgaard A., Fensholt R., Jensen K.H. 2008. Combining the triangle method with thermal inertia to estimate regional evapotranspiration – Applied to MSG-SEVIRI data in the Senegal River basin. Remote Sensing of Environment. Vol. 112(3) p. 1242–1255. DOI 10.1016/j.rse.2007.08.013.

Tang R., Li Z.L. 2015. Evaluation of two end-member-based models for regional land surface evapotranspiration estimation from MODIS data. Agricultural and Forest Meteorology. Vol. 202 p. 69–82.

Teixeira A.D.C., Bastiaanssen W.G., Ahmad M.U.D., Bos M.G. 2009. Reviewing SEBAL input parameters for assessing evapotranspiration and water productivity for the Low-Middle Sao Francisco River basin, Brazil: Part A: Calibration and validation. Agricultural and Forest Meteorology. Vol. 149(3–4) p. 462–476. DOI 10.1016/j.agrformet.2008.09.016.

Timmermans W.J., Kustas W.P., Anderson M.C., French A.N. 2007. An intercomparison of the surface energy balance algorithm for land (SEBAL) and the two-source energy balance (TSEB) modeling schemes. Remote Sensing of Environment. Vol. 108(4) p. 369–384. DOI 10.1016/j.rse.2006.11.028.

USGS undated a. Earth Explorer. [online]. United States Geological Survey [Access 19.10.2016]. Available at: http://earthexplorer.usgs.gov

USGS undated b. Landsat Missions [online]. United States Geological Survey [Access 05.03.2022]. Available at: https://www.usgs.gov/landsat-missions/landsat-8

Van de Griend A.A., Owe M. 1993. On the relationship between thermal emissivity and the normalized difference vegetation index for natural surfaces. International Journal of Remote Sensing. Vol. 14(6) p. 1119–1131. DOI 10.1080/01431169308904400.

Vidal A., Perrier A. 1990. Irrigation monitoring by following the water balance from NOAA-AVHRR thermal infrared data. IEEE Transactions on Geoscience and Remote Sensing. Vol. 28(5) p. 949–954. DOI 10.1109/36.58984.

WWAP 2012. Managing water under uncertainty and risk: The United Nations World Water Development Report 4. Paris, France. UNESCO World Water Assessment Programme pp. 886.

Zou M., Zhong L., Ma Y., Hu Y., Huang Z., Xu K., Feng L. 2018. Comparison of two satellite-based evapotranspiration models of the Nagqu River Basin of the Tibetan Plateau. Journal of Geophysical Research: Atmospheres. Vol. 123(8) p. 3961–3975. DOI 10.1002/2017JD027965.